Characterization of laser-induced plasmas as a complement to high-explosive large-scale detonations

Clare Kimblin, Rusty Trainham, Gene A. Capelle, Xianglei Mao, and Richard E. Russo

Citation: AIP Advances **7**, 095208 (2017);
View online: https://doi.org/10.1063/1.4999793
View Table of Contents: http://aip.scitation.org/toc/adv/7/9
Published by the American Institute of Physics

Characterization of laser-induced plasmas as a complement to high-explosive large-scale detonations

Clare Kimblin,[1,a] Rusty Trainham,[1] Gene A. Capelle,[1] Xianglei Mao,[2] and Richard E. Russo[2]
[1]*National Security Technologies, LLC, Special Technologies Laboratory, Santa Barbara, CA 93111, USA*
[2]*Lawrence Berkeley National Laboratory, Berkeley, CA 94720, USA*

(Received 3 May 2017; accepted 30 August 2017; published online 12 September 2017)

Experimental investigations into the characteristics of laser-induced plasmas indicate that LIBS provides a relatively inexpensive and easily replicable laboratory technique to isolate and measure reactions germane to understanding aspects of high-explosive detonations under controlled conditions. Spectral signatures and derived physical parameters following laser ablation of aluminum, graphite and laser-sparked air are examined as they relate to those observed following detonation of high explosives and as they relate to shocked air. Laser-induced breakdown spectroscopy (LIBS) reliably correlates reactions involving atomic Al and aluminum monoxide (AlO) with respect to both emission spectra and temperatures, as compared to small- and large-scale high-explosive detonations. Atomic Al and AlO resulting from laser ablation and a cited small-scale study, decay within ~10^{-5} s, roughly 100 times faster than the Al and AlO decay rates (~10^{-3} s) observed following the large-scale detonation of an Al-encased explosive. Temperatures and species produced in laser-sparked air are compared to those produced with laser ablated graphite in air. With graphite present, CN is dominant relative to N_2^+. In studies where the height of the ablating laser's focus was altered relative to the surface of the graphite substrate, CN concentration was found to decrease with laser focus below the graphite surface, indicating that laser intensity is a critical factor in the production of CN, via reactive nitrogen.
[http://dx.doi.org/10.1063/1.4999793]

I. INTRODUCTION

Large-scale high explosive (HE) field tests, conducted at the Nevada National Security Site and other locations, provide data for optical[1] and radio frequency[2,3] (RF) models of detonation environment emissions. The tests are data rich, but are expensive and time consuming. Collection of high spatial and temporal resolution optical data in the field is complicated by substantial blackbody radiation backgrounds, optical obscurants (such as smoke), long path lengths and associated self-absorption of emitted radiation. Long detector gate widths also are required to collect signals attenuated as a result of large stand-off distances. By contrast, smaller-scale laboratory explosions provide a complementary or alternative approach. Detonations performed in highly instrumented semi-enclosed bays[4] and explosive test chambers[5–11] provide a means to study many of the physical and chemical processes associated with HE events. For instance, Carney et al. investigated a fuel-rich aluminized explosive detonated in vacuum and different bath gases.[6–8] Temporal optical emissions revealed that cyano radical (CN), C_2 radical, and atomic aluminum (Al) emissions appear at early times, with aluminum monoxide (AlO) appearing at later times. High-resolution studies of

[a]Corresponding author. Electronic mail: kimblicw@nv.doe.gov (C. Kimblin).

conventionally detonated thin film hexanitrostilbene samples were recently performed to aid observation of reactive intermediates that could be obscured in larger reacting samples.[11] In the first hundreds of ns, CN ($B\ ^2\Sigma^+ \rightarrow X\ ^2\Sigma^+$) is observed with rotational and vibrational excitation temperatures higher than those expected based on thermochemical estimates of detonation temperature (~10,000 K vs. 3600 K–3700 K). Small scale tests in explosive test chambers[12,13] or benchtop laser ablation platforms[14–19] have permitted the use of shock wave imaging techniques (schlieren and shadowgraphy) which can be coupled with spectroscopic techniques, to observe shock waves initiated by the laser pulse and associated emissive species. More recently, using laser ablation of a series of explosives with schlieren imagery, Gottfried has demonstrated that there is a strong correlation between an explosive's measured performance, based on full-scale detonation testing, and its measured shock wave propagation velocity.[15]

A microscopic version of an explosion is created when a high-power nanosecond laser pulse impacts a tiny spot on target (typically a few hundred microns in diameter). Plasma temperatures over 10,000 K (as high as 40,000 K[20]), pressures up to 10^5 atmospheres,[21] and shock waves are produced. As the plasma cools, ionic and atomic elemental constituents can be discerned, followed by formation of gaseous molecular products.[21,22] Laser ablation can be performed using a single pulse to study a single event, or at high repetition rates (from 1 Hz to 50 kHz[23]) and the shots integrated for high signal-to-noise ratio. The plasma and shock waves are on the millimeter scale and altering ablation environments is readily feasible with a small gas-tight chamber. The technique permits temporal characterization of excited state ions, atoms and molecules associated with early species formation, in addition to those that may be produced as a result of later time combustion. Extraction of electron density from emission line profiles, and temperature from line intensities and/or molecular band structure also is feasible.[24–28]

In this work the use of high temporal resolution Laser-induced Breakdown Spectroscopy (LIBS) of Al, graphite and air is explored as a less labor- and time-intensive benchtop technique to generate optical signatures that mimic aspects of explosive detonations. With graphite and air, shadowgraphy is combined with optical spectroscopy. Aluminum was studied (Section III.A) because it can be used as a propellant and/or casing, and it was used as a casing at a recent HE field test. Graphite was studied (Section III.B) because it is predicted as a major HE detonation product,[29] and modelers are interested in understanding the effect of carbon on HE tests. Air ionized by a focused laser was studied (also in Section III.B) because significant air ionization results from high thermal temperatures (T ~11,000 K) generated by HE detonation product shock waves.[30] In this work and others'[16,31] species produced by laser-sparked air (N_2^+, N_2, N-I, N-II, O-I, O-II) correspond to a number of those predicted by models of high temperature air (1000 K < T < 24,000 K).[32] CN is also a major spectral component observed in air plasma created with an inductively coupled torch[33] and in laser-sparked air plasma, as reported by Harilal et al.[16] and herein. Emission from species associated with shock wave–generated thermal excitation of air is thought to contribute to the RF signals (kHz to GHz) recorded at large scale HE field tests.[2,3,18,34,35] Results from optical studies of laser-induced plasmas that are pertinent to (1) aiding test and evaluation of HE field diagnostics that are better able to detect species and provide temperatures relevant to optical and RF simulations, (2) informing field collection parameters and analysis methods, and (3) ultimately providing empirical data of interest to modelers, are discussed.

II. EXPERIMENTAL DETAILS

A schematic of the LIBS and shadowgraph setup is shown in Fig. 1. A 1064 nm, pulse width 12 ns, Nd:YAG laser (Big Sky Laser Technologies, model CFR400) was used with a 125 mm focal length beam focusing lens for ablation of samples or for air breakdown. The gas-tight chamber was either under vacuum (base pressure 1×10^{-6} Torr) or back-filled with air or argon. The resulting laser-induced plasma was imaged (demagnified to 85% of its true size) by a 60 mm focal length lens onto a 1.1 mm diameter bundle of 19 close-packed 200 μm core (silica on silica, high OH) fibers. This bundle was mounted on a micrometer-controlled translation stage to allow different portions of the image to be analyzed. The other end of the bundle was terminated in a line of fibers, imaged into a f/4.1 spectrograph (Horiba, iHR320) with 320 mm focal length, equipped with 2400, 1200, and 150 g/mm gratings. These provided typical spectral resolutions of 0.18, 0.3, and 2.6 nm, respectively.

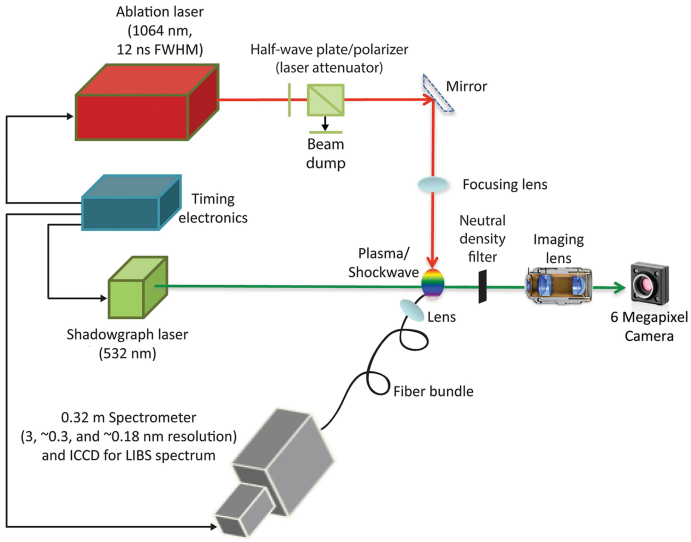

FIG. 1. Schematic of LIBS and shadowgraphy setup.

The detector mounted to the spectrograph was an intensified CCD (ICCD) system (Andor, "iStar") that is sensitive from 200 to 800 nm; this detector allowed both amplification of weak signals and precise timed gating (down to about 10 ns gate widths).

A second independently controlled Nd:YAG laser (Big Sky Laser Technologies, model CFR400), frequency doubled to 532 nm and with a similar 12 ns pulse width, was incorporated into the system for imaging shadowgraphs of the laser-induced plasma at various delay times. The expanded 532 nm beam (14 mm diameter at the target zone) was sent across the laser-induced plasma, perpendicular to the 1064 nm pulse direction, and into a camera (Nikon D-50 fitted with 500 mm lens and extension tube) located approximately 1.13 meters distant from the laser ablation site. Most of the interference (background) light emitted from the plasma was eliminated using a 532 nm bandpass filter and an OD = 3 filter in front of the camera. Shadowgraphy provided images of shock waves, and was used to track shock wave velocity in graphite and air-spark experiments, and as a means to observe shock wave propagation as a function of laser focus relative to the graphite substrate. To show the size of plasma light emitted over its measurable light-emitting duration, in relation to the shock wave at a particular time, the 532 nm bandpass filter was removed from the front of the camera, and the OD filter (normally positioned between the sample chamber and the camera) was positioned between the shadowgraph laser and sample chamber. In this way there was less attenuation of the plasma spark, which could then be seen as a pinkish light by the near-IR sensitive camera, and the shadowgraph appeared as a green image corresponding to the selected time delay. Laser fluence on the sample surface could be controlled by adjusting the height of the ablation laser focusing lens. By increasing the height of the laser focus above the sample in air, it could be seen by shadowgraphy that more air was sparked with the focus further above the sample.

Solid targets were in the form of Al metal (Alfa Aesar P/N 43429, 99.9995% purity) and graphite rods (McMaster-Carr, conductive graphite) that could be rotated or translated in the chamber to achieve a fresh ablation spot. In our experiments, a 35 mJ/pulse (for most Al experiments) to 55 mJ/pulse (for graphite and sparked air) 1064 nm ablating laser pulse was focused onto the target (as well as above and below the surface of the graphite). The laser beam was ~8 mm in diameter upon going into the 125 mm focusing lens, and a single pulse focused at the surface of an Al sample produced a ~200 μm diameter spot. Spectra collected in the field, from a large-scale detonation of HE with an aluminum case (shown in Fig. 3a) were collected through a telescope fiber-coupled to an Ocean Optics USB2000+ spectrometer with 1.2 nm spectral resolution and 2 ms integration times. Before temperature simulations were performed the LIBS and Ocean Optics spectra were flat-field corrected for detector response using calibration lamps (Gooch and Housego, OL 245-M and OL FEL-C respectively).

III. RESULTS AND DISCUSSIONS

A. Al laser ablation compared to explosive test chamber and large scale detonation of Al-encased explosive

1. Al species observed and temporal dependence

To demonstrate concordance and differences between laser-induced plasmas and explosions generated by HE charges, Al species produced by laser ablation of aluminum in our lab (Fig. 2a) were compared to the decay of those produced by the detonation of 20 grams of aluminized explosive (PBXN-113) in an explosive test chamber (Fig. 2b).[6] PBXN-113 data were recorded using a streak camera. In spite of the different methods used for their generation, there are considerable similarities in the decay rate of neutral, atomic aluminum (Al-I: 394.40 nm, 396.15 nm, $3s^2 4s\ ^2S \rightarrow 3s^2 3p\ ^2P^0$ transition) and the growth and decay of aluminum monoxide AlO. In both cases, neutral Al decays exponentially as AlO is formed, with Al-I decaying from highest intensity immediately after ablation/detonation to nearly 0 in roughly 5 to 10 μs. With both platforms AlO appears at ~2 μs after ablation/detonation, and under our experimental conditions emission decays over a period of approximately 20 μs following laser ablation, and 25 μs after detonation of PBXN-113. With respect to the observed differences at the earliest stage (ns) it is noted that Al-I produced by laser ablation decays at a faster rate than that generated in the explosive test chamber. At early times it is expected that differences will be highlighted due to the higher temperature and enhanced ionization in the laser plasma, vs. detonated PBXN-113. Using integrated peak intensities for two singly ionized Al-II lines ($3s4f\ ^3F^0 \rightarrow 3s3d\ ^3D$ transition at 358.7 nm and $3s4p\ ^1P^0 \rightarrow 3p^2\ ^1D$ transition at 466.3 nm), and assuming a Boltzmann distribution, the electron excitation temperature was calculated to be ~30,000 K at 50 ns using the line pair method.[36] By 2 us, T ~ 4400 K, as calculated from the AlO emission (see Section III.2). In contrast, peak temperatures recorded by 3-color pyrometry at light breakout in PBXN-113 experiments are typically on the order of 4000 K.[8]

In Fig. 3 time-resolved spectral data collected following detonation of an Al-cased explosion in the field is compared to that collected following benchtop laser ablation of Al in air. Atomic Al and AlO emissions are both observed but their timing differs. In the HE field test, Al-I and AlO are observed in the ms range, whereas in the lab they are seen in the nanosecond-to-microsecond range. In the HE field test there is significant blackbody emission. This comes from hot smoke and other entrained particulates, as well as scattered solar blackbody radiation. Temperature-broadened molecular emissions may also contribute to the blackbody observed in the field spectra. In addition to the scales of the experiments (nanograms of Al ablated over a ~10 ns period in the lab, vs. ~kilograms of Al in a longer duration explosive detonation in the field), factors such as Al particle sizes produced and the timing of oxygen depletion (during the explosive burst with HE) followed by replenishment due to turbulent mixing of air, will all contribute to differences in timescales.

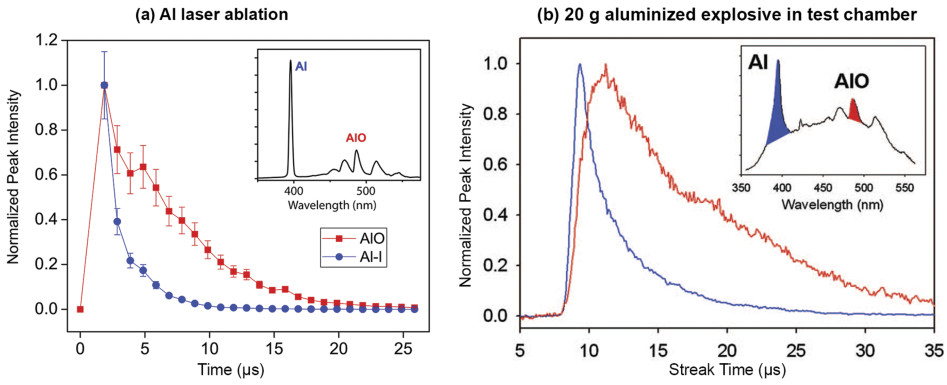

FIG. 2. Al-I and AlO optical signatures as a function of delay time generated by (a) laser ablation of Al, inset shows emission at 1.86 μs and (b) detonation of a 20 g aluminized explosive in an explosive test chamber, Reprinted with permission from Carney *et al.*, "Time-resolved optical measurements of the post-detonation combustion of aluminized explosives," Rev. Sci. Instrum. **77**, 063103-1–063103-6 (2006). Copyright 2006 AIP Publishing LLC.

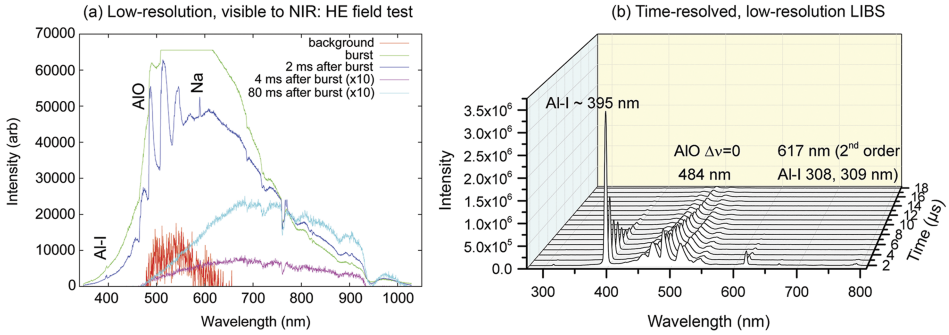

FIG. 3. (a) Raw data from large-scale HE field test vs. (b) laser-induced Al plasma. Al species generated by laser ablation appear in the large-scale HE field test with an Al shell at 2 ms after the burst. Second order Al-I lines seen with laser ablation at ~617 nm correspond to Al-I emissions (at 308 and 309 nm) observed 5 ms after the explosive burst using a UV modular spectrometer in the field.

2. Temperature derivations from AlO emission

AlO is formed from gaseous (g) neutral aluminum (Al(g)) as indicated in Equations 1 and 2 below. The reaction is in cooperation or competition with oxygen (O) recombination. Equation 1 requires molecular oxygen whereas Equation 2 requires atomic oxygen.

$$Al(g) + O_2 = AlO + O \tag{1}$$

$$Al(g) + O + M = AlO + M \tag{2}$$

The temperature at which AlO formation is favored by the chemical reactions in Eqs.1 and 2 is ~4300 K.[37] The ro-vibrational temperature of the laser-induced plasma ~2 μs following ablation is 4400 ±100 K (see Fig. 4a). This temperature was derived from a least squares fit of the flat-field corrected spectral data to a molecular band model for the $\Delta\upsilon = -1$ AlO band ($B\ ^2\Sigma^+ \rightarrow X\ ^2\Sigma^+$ transition). The intensity of each ro-vibrational line was calculated using parameters (such as rotation-vibration line energy levels and Einstein A coefficients (A_{ij})) which were derived from direct numerical solution of the Schroedinger equation by Patrascu et al.[38] A Lorentzian line width function was applied to each transition line, and the lines were summed to simulate the spectrum of interest using a procedure described by Dong et al.[39]

AlO emission observed in the field immediately after the burst could not be fit due to detector saturation. However, at ~2 to ~4 ms after the burst, AlO emission ($B\ ^2\Sigma^+ \rightarrow X\ ^2\Sigma^+$) was prominent and the detector was not saturated. Using a flat-field corrected field spectrum, simulations were performed to determine a spatially and temporally integrated temperature. It was first necessary to use a polynomial fit to subtract the blackbody background. Two temperatures of 2509 K (91%) and 6822 K (9%) were found to best fit the blackbody emission; possibly accounting for the explosive temperature, with high temperature contributions from solar reflection and shocked air. When fitting the full $B\ ^2\Sigma^+ \rightarrow X\ ^2\Sigma^+$ $\Delta\upsilon = -3$ to $\Delta\upsilon = +3$ emission, the program and least squares fitting used to fit the laser ablation–generated AlO, was modified to account for AlO self-absorption within the macro-scale, approximately 10 m diameter, plume. After consideration for self-absorption, the emission intensity for each ro-vibrational line is:

$$I = I_0 exp\,(-\tau) \tag{3}$$

Where I_0 is the simulated emission intensity of molecular lines before self-absorption, and τ is the optical depth of the absorbing layer at the line center, calculated as:[40]

$$\tau = \frac{1}{8\pi}\sqrt{\left(\frac{m}{2\pi k_B T}\right)}\lambda^3 A g_u \frac{n_{AlO} L}{Q} exp\left(-\frac{E_l}{k_B T}\right) \tag{4}$$

Where m is mass of AlO molecules, T is temperature, λ is wavelength, A is the Einstein coefficient of spontaneous emission, g_u is the statistical weight of the upper energy level, n_{AlO} is the number density of AlO, L is the characteristic length of the plume, Q is the partition function of AlO molecules, E_l is the lower energy level of the emission line, and k_B is the Boltzmann constant.

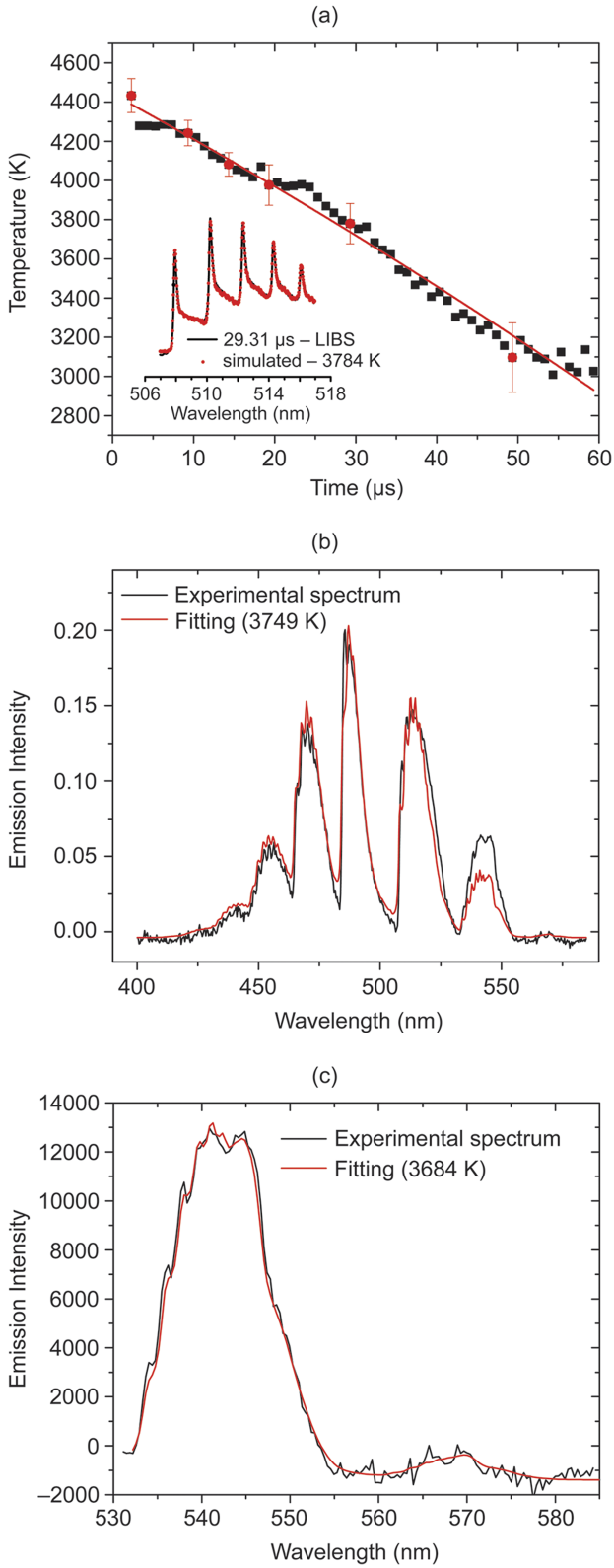

FIG. 4. (a) Temperature vs. time determined from AlO B-X $\Delta\upsilon = -1$ vibrational band, produced via laser ablation of Al. Inset shows the lab spectrum at ~29 μs and simulated fit (red circles) overlaid. (b) Optimal fitting of the large-scale field spectrum bands between 400 nm and 485 nm, with self-absorption taken into account, indicates a time- and spatially-integrated temperature of 3749 K. (c) Fitting of just the $\Delta\upsilon = -2$ and $\Delta\upsilon = -3$ bands of the field spectrum, without self-absorption, indicates a temperature of 3684 K.

The B $^2\Sigma^+ \rightarrow$ X $^2\Sigma^+$ bands between 400 nm and 585 nm were fit with self-absorption taken into consideration. A temperature of 3749 K (Fig. 4b) shows good correspondence over the $\Delta\upsilon = 3$ to $\Delta\upsilon = -1$ bands, but not the $\Delta\upsilon = -2$ and $\Delta\upsilon = -3$ bands. This may be a function of insufficient self-absorption compensation. Of the B $^2\Sigma^+ \rightarrow$ X $^2\Sigma^+$ bands, the $\Delta\upsilon = -2$ and $\Delta\upsilon = -3$ bands are least susceptible to self-absorption.[9] The optimal fit for the $\Delta\upsilon = -2$ and $\Delta\upsilon = -3$ bands, without accounting for self-absorption, was found to be 3684 K (Fig. 4c). Taking the two fitting methods into account, it is estimated that the spatially integrated temperature in the field was approximately 3700 K at ~2 to ~4 ms after the burst.

The simulated temperature for AlO in the HE field test at ~2 to ~4 ms is lower than that determined for AlO following laser ablation, and the peak temperatures recorded by 3-color pyrometery at light breakout in the explosive test chamber with PBXN-113 (roughly 4000 K[8]). Observation of a lower spatially integrated temperature in the field is not unexpected, because some cooling will have occurred between the time when AlO is first observed (in the ~0 to ~2 ms saturated spectrum) and the time when the ~2 to ~4 ms spectrum was collected. In the case of the field test, there may also be a radiative cooling mechanisms due to heat exchange with soot/carbon nanoparticles generated in the field. As seen in Fig. 4a, with LIBS, AlO cooled to ~3700 K after roughly 30 μs.

3. LIBS of Al; effects of oxygen removal and decreased pressure

Turbulent mixing with oxygen is another parameter that can influence the rate at which AlO burns, whether on the benchtop[17] or in the field. We controlled the overall availability of oxygen for combustion with ablated aluminum by changing the bath gas. In comparing the decay of Al-I in vacuum, air, and argon (Fig. 5) it is seen that the decay of Al-I is faster in air than in argon (a comparatively dense but inert gas). In vacuum, the apparent rapid decay of Al-I is due to fast plasma expansion; however, in air the availability of oxygen for aluminum combustion opens a chemical reaction pathway for the formation of AlO. One can see that the decay of Al-I is accompanied by the appearance of AlO in Fig. 5. There are essentially two sources of AlO in the plasma, one from the fracturing of the Al_2O_3 passivation layer on the aluminum surface, this is expected to be a minor constituent. The second is the combustion of elemental aluminum. AlO derived from the passivation layer was observed in vacuum early in the plasma evolution. Piehler et al.[41] have also been identified it in N_2 and He bath gases, in the absence of ambient O_2. In argon however, definitive identification of early-time AlO could not be made due to interfering argon emission lines. Combustion derived AlO is only available when oxygen is present and temperatures and pressures favor the chemical

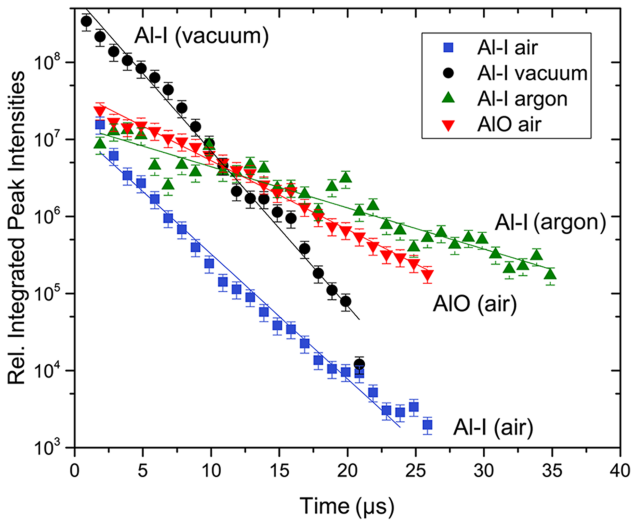

FIG. 5. Comparison of the decay of Al-I in vacuum, air, and argon using the integrated peak intensity from Al atomic lines at 394.40 nm and 396.15 nm ($3s^24s\ ^2S \rightarrow 3s^23p\ ^2P^0$ transition), and the decay or AlO in air. The decay rate of atomic Al is faster in air than in argon, and is accompanied by the appearance of AlO in air (AlO intensity was obtained by integrating over AlO B-X bands $\Delta\upsilon = +1$ to -1). In vacuum, rapid Al-I decay is influenced by the lack of plasma confinement.

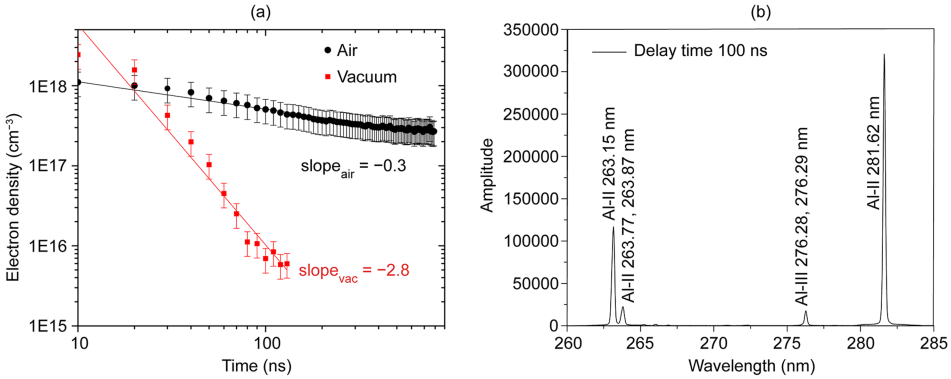

FIG. 6. (a) The influence of pressure on electron density, calculated using the line width of the 3s4s 1S -> 3s3p $^1P^0$ transition of the Al-II ion at 281.6 nm. (b) Al emissions in vacuum at 100 ns, between 260 nm and 285 nm. The strongest emission appears at 281.6 nm.

pathways from Al-I to AlO. Two distinct radiance intensity peaks collected by us at an HE field test (not shown here) suggest that oxygen depletion during an explosive blast may extinguish combustion and that subsequent turbulent in-welling of air can restart it.

The lack of plasma confinement in vacuum relative to air is also demonstrated in a plot of electron density vs. time using the 3s4s ^1S -> 3s3p $^1P^0$ transition of the Al-II ion in the UV, at 281.6 nm (Fig. 6). The electron number density can be derived from line width and Stark constants.[24] The Stark-width constant was derived from the work of Konjević et al.[42] In vacuum, the electron density decays with a slope of –2.8, suggesting free expansion of the plasma, whereas in air the decreased decay rate (slope –0.3) indicates plasma confinement. If sufficient spectral resolution is available in the field, then a correlation between electron density decay and RF emissions may be observed.

In Fig. 7, ionic and atomic Al species observed with laser ablation in vacuum and air are compared on the nanosecond timescale. Doubly ionized Al, Al-III, could be observed in vacuum over a range of times, but was observed in air only briefly (at ~40 and ~50 ns); Al-II was significantly more predominant in air. At the HE field test, ionic Al species were not observed. This may be due to the lower excitation temperatures in the field. It is also likely that with millisecond gate widths, shorter duration ionic emissions are masked by the strong blackbody background. Even if not observed optically, pathways involving ionic Al may contribute to early-time RF signatures in the field.

B. Graphite and sparked-air laser ablation experiments

Models predict graphite as the most abundant detonation product for a number of explosives, including TNT,[29] but its effect on HE field tests is not yet understood. Laser ablation studies were

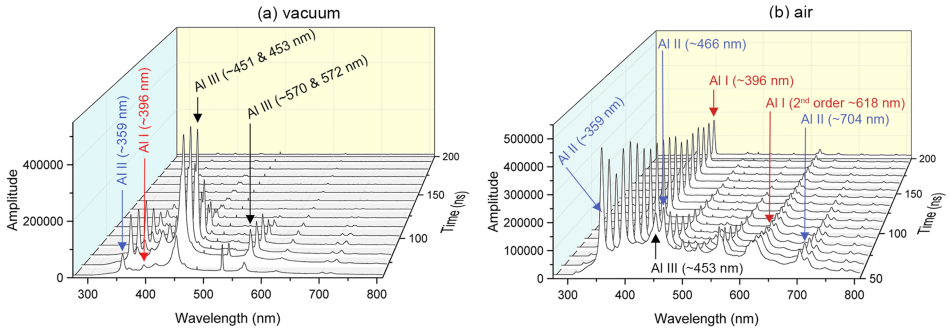

FIG. 7. Time-resolved traces at 10 ns intervals, with early time emissions stronger than later time emissions, and highly charged species decaying to lower charged and atomic species at later times. (a) In vacuum, free expansion permits persistence of Al-III species in the 60–200 ns range, whereas (b) at 60 ns and beyond in air, Al-II is the most highly ionized species observed.

therefore performed with the objective of providing some insight into the role of graphite in HE phenomena; and to provide examples of spectroscopic signatures that may be measurable in the field. These laser ablation studies compare the species and temperatures produced by air break down, with and without ablated graphite present. The formation of atomic and molecular species as a function of laser focus at, above, and below the surface of a graphite substrate was also compared.

1. Sparked-air vs. laser ablated graphite in air – Emissive components and plasma temperature derivation

Following laser sparking of air, and laser ablation at the surface of a graphite substrate, time-resolved spectra (Figs. 8a and 8b) show that atomic O, nitrogen (N), and hydrogen (H) are present due to air breakdown. The intensity of these species decays rapidly. In the absence of graphite, N_2^+ is the predominant emitting molecular species, whereas with graphite, CN radical is predominant. In Figs. 8c and 8d shock wave images produced following laser sparking of air and following laser ablation with the laser focus just above the graphite surface are shown. The pinkish light corresponds to plasma light emitted over its light-emitting lifetime in relation to the shock wave at 300 ns. The magnitude of plasma light emitted over its entire light-emitting lifetime is smaller than the shock wave at 300 ns delay time. By 10 μs, shock waves (not shown) have expanded to a ~12 mm diameter sphere (without graphite) and a ~13.5 mm diameter sphere (with graphite), indicating average shock wave velocities on the order of ~5 km/s at 300 ns vs. ~1 km/s at 10 μs. Using a series of 10 shock-waves collected between 5 ns and 10 μs, without plasma light, instantaneous shock wave velocities (Fig. 9) were calculated by taking the first derivative of the shock wave width with respect to time. Open squares represent shock wave instantaneous velocity generated by sparked air, and circles

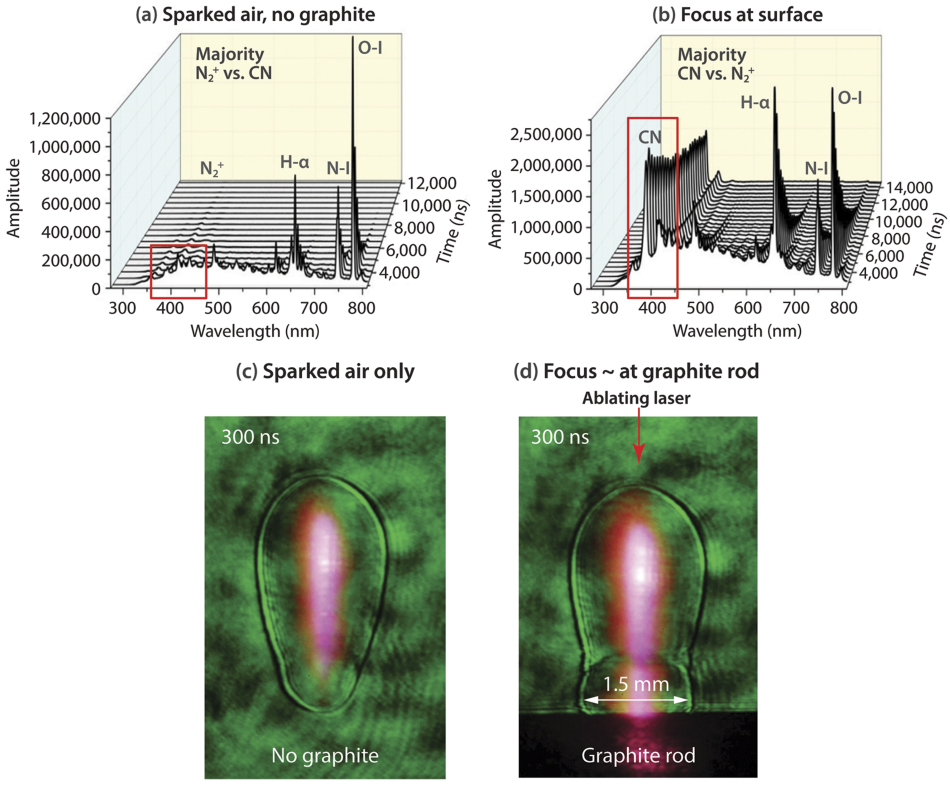

FIG. 8. Time-resolved LIBS spectra (a) of sparked air with no graphite and (b) with the laser focus at the surface of a graphite rod. Red boxes indicate the approximate region used for temperature determination at 10 μs. Plasma light over its light-emitting lifetime (pink) and shock wave images at 300 ns (c) in air and (d) with laser focus approximately at the surface of the graphite substrate. The shock waves were ~1.5 mm laterally at 300 ns.

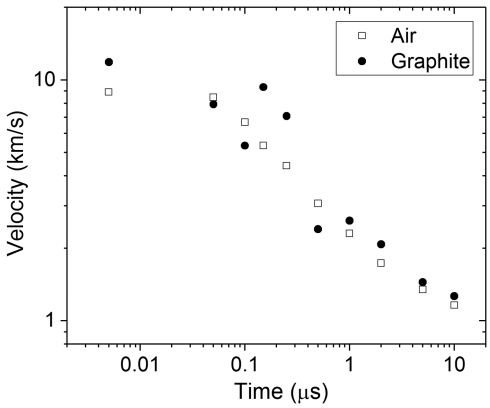

FIG. 9. Instantaneous velocity vs. time calculated from shock wave widths: for sparked air, and graphite ablated with the laser focus at the substrate surface.

are from laser ablation with the focus at the graphite surface (as shown in Fig. 11c and 11d shadowgraphs). With sparked air and with the graphite substrate, initial velocities are on the order of 10 km/s, by 10 μs velocities have dropped to just over 1.0 km/s. The behavior of the graphite shock wave appears to be more erratic than that of the air shock wave.

Emissive components and estimated plasma temperatures were determined at a 10 μs gate delay with and without graphite present using the 362–453 nm spectral region, collected with a 2400 g/mm grating at center wavelengths of 378 nm and 425 nm, and 500 ns gate width. The estimated plasma temperature indicates the best representative temperature based on molecular species, for the series of temperatures actually encompassed in the collection region. With ablated graphite, this will include carbon particulates cooling at different rates. SPECAIR[43] software was used for temperature simulation and molar ratio determination. To account for instrumental broadening, simulated spectra were convolved with a slit function collected using an argon line at 394.9 nm at the experimental slit widths. Experimental spectra are shown in black in Figures 10a and 10b, with simulated spectra overlaid in red. In the 362 to 453 nm region CN violet $\left(B\,^2\Sigma^+ - X\,^2\Sigma^+\right)$ and $N_2{}^+$ first negative system $\left(B\,^2\Sigma_u^+ - X\,^2\Sigma_g^+\right)$ emissions are predominant.

With the optical fiber positioned toward the base of the air-spark, for air-spark experiments, and near the surface of the graphite rod for graphite experiments, the concentration of CN observed in the presence of graphite was more than 50x higher. Plasma temperatures, with and without graphite, (assuming local thermodynamic equilibrium) ranged from 6700 K to 8000 K, with plasma

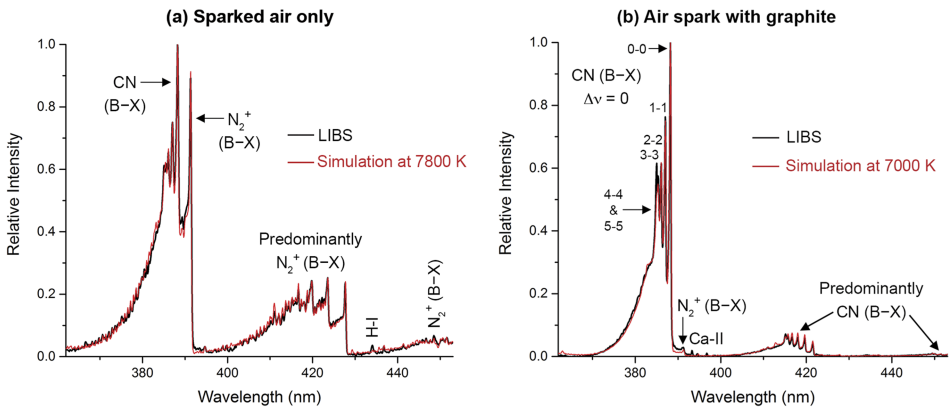

FIG. 10. LIBS spectra (black lines) (1064 nm ablation [~55 mJ], 500 ns gate width and 10 μs delay) overlaid by temperature simulations (red lines) for (a) air spark only and (b) air spark with graphite (predominantly CN ($B\,^2\Sigma^+ \rightarrow X\,^2\Sigma^+$) $\Delta\upsilon = 0$ bands, are labeled). Calcium (Ca) is an impurity in graphite.

temperatures for the graphite plasma lower than those for sparked air alone. In addition to CN and N_2^+, both simulations included atomic O and N radicals. With graphite present, C_2 was additionally observed between 423 and 474 nm (full range not shown here), and included in the fit (ratio of N_2^+:C_2:CN ~ 1:1.5:20).

Simulations for the region of sparked air observed in the 362–453 nm spectral range suggest that the plasma temperature was over 7700 K. In Fig. 10a, a simulated spectrum with T = 7800 K is overlaid in red. The ratio of N_2^+ to CN is roughly 5:1 even though the carbon content in air is just 0.04 %, from CO_2, vs. 78% nitrogen. The sparked air plasma temperature, and prominence of CN is similar to that observed by Harilal et al.[16] With graphite present, optimal SPECAIR fits in the 362–453 nm spectral range suggest a lower plasma temperature than that predicted for the sparked-air-only experiment, closer to 7000 K, with the N_2^+ to CN ratio roughly 1:20. In Fig. 10b a simulated spectrum with T = 7000 K is overlaid in red. These results suggest that the higher than expected rotational and vibrational excitation temperatures observed with conventionally detonated thin film hexanitrostilbene samples[11] (~10,000 K in the first hundreds of ns, estimated from CN ($B\ ^2\Sigma^+ \rightarrow X\ ^2\Sigma^+$) simulations, vs. 3600 K–3700 K based on thermochemical estimates of detonation temperature) could be related to shock wave–generation of CN in air.

a. Discussion of CN ($B\ ^2\Sigma^+ \rightarrow X\ ^2\Sigma^+$) simulation vs. experimental fit for graphite. While there is a good fit for the CN violet $\Delta\upsilon = 0$ sequence 0-0, 1-1, 2-2 and 3-3 band heads, it was not possible to fit the 4-4 and 5-5 band heads as successfully. Similarly, Boubert et al. examined five sets of spectroscopic constants in attempts to reproduce an experimental spectrum they derived from a DC arc and graphite electrode. They determined that the CN violet $\Delta\upsilon = 0$ sequence was not in very good agreement with the experimental spectrum for quantum numbers greater than 4.[44] This may be related to the pathways in which the CN is generated. In laser ablating five different organic materials, Fernandez-Bravo et al.[45] observed that at early times (delay of 500 ns) the vibrational distribution of CN $\Delta\upsilon = 0$ sequence bands was material dependent. With PVC and Teflon, $\Delta\upsilon = 4\text{-}4$ transitions were more intense than $\Delta\upsilon = 3\text{-}3$, 2-2, and 1-1 bands. They suggested that competitive routes for generation and quenching of CN may co-exist and that these may result in alternative excitation pathways that modify the vibrational emission. The graphite plasma observed spectroscopically will also contain fragments of non-homogeneous particles (carbon clusters) of various sizes. These will cool at differing rates, thereby creating non-homogenous temperature regions that may in turn affect the formation of CN, and temperatures of the molecular and atomic species observed spectrally.

For graphite ablated in vacuum, Harilal et al.[46] captured ICCD images of what they described as a delayed (>5 μs) firework-like emission that peaked between around 20–30 μs after the onset of plasma. They attribute this to ejected hot particles or droplets formed by overheating of trapped gases in the layered graphite structure. Dinescu et al.[47] reported on the laser ablation of graphite and temperatures derived from the CN $\Delta\upsilon = 0$ sequence, as a function of position above the substrate, nitrogen gas pressure (1–250 Pa) and laser fluence. Their spectral simulations indicated that temperatures varied as a function of distance above the substrate and that rotational and vibrational temperatures were not the same (rotational temperatures were higher than vibrational temperatures closer to the substrate, but lower than vibrational further away). The variation in temperature along the vertical axis of the plasma was attributed to CN production via reaction of atomic nitrogen with carbon clusters of different mass. More recent laser-induced plasma studies with graphite[48] and carbon isotopic ratio studies of C_2 and CN indicate that C_2 is not a precursor for CN formation, and that CN formation likely involves atomic carbon, or species with a single carbon atom.[49]

Uncertainty associated with temperature simulations will include contributions based on determination of optimal concentrations from all emitting molecules and atomic species in the spectral region being fit. To ensure that the simulated fits were good over a broader spectral range, SPECAIR simulated spectra were compared to experimental spectra collected beyond 453 nm. SPECAIR simulations also permit calculation of non-thermal equilibria, self-absorption, and plasma emission at higher pressures. In varying these parameters there were no indications that accounting for possible self-absorption, non-thermal equilibrium, or higher pressures provided better fits. Inclusion of energetic electrons also did not account for the stronger emission in the $\Delta\upsilon = 4\text{-}4$ and 5-5 bands with graphite present.

2. Varying the position of laser focus relative to the graphite substrate

To explore the relationship between emitting species and the position of maximum laser energy density relative to a graphite substrate in air, the laser focus above the graphite surface was altered and temporal emission of species was compared. Shadowgraphy indicates that with the focus 2 mm above the surface, air and graphite are sparked individually, prior to the shock waves fusing together (Figs. 11a at 50 ns and 11b at 250 ns). With the focus at the surface, air is still entrained in an axially elongated shock-wave (Fig. 11c at 50 ns, 11d at 250 ns). With the focus below the surface the shock wave is less axially elongated, suggesting that less air is entrained (Figs. 11e at 50 and 11f at 250 ns).

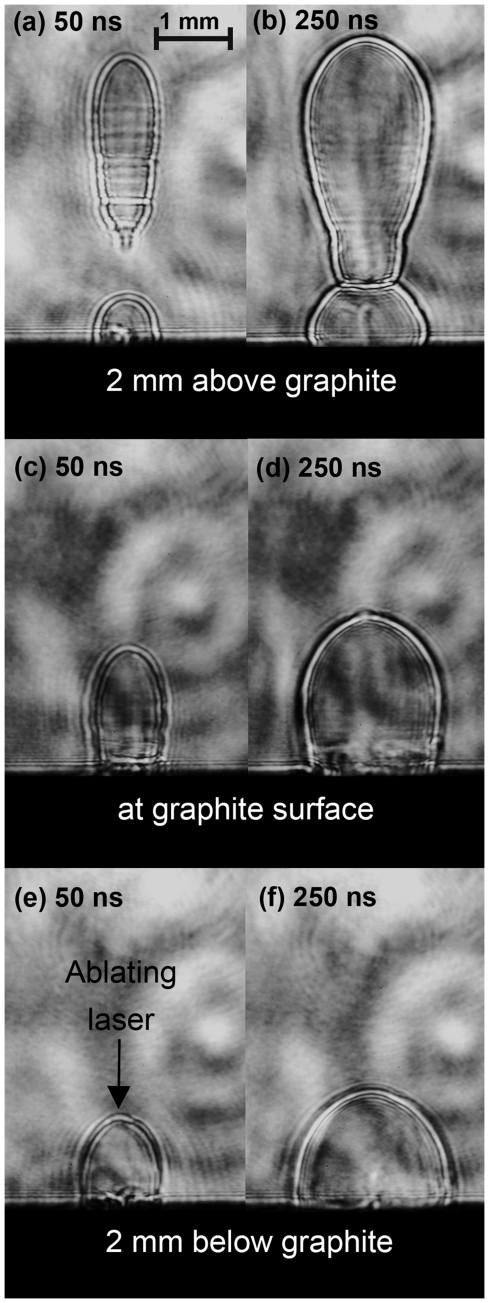

FIG. 11. Representative shock wave images at 50 ns (left columns) and 250 ns (right columns) with the focus 2 mm above the graphite substrate (a and b), at the surface of the substrate (c and d), and 2 mm below the graphite substrate (e and f). With the focus 2 mm above the graphite, air and graphite shock waves begin to fuse at 250 ns (b).

This is supported by spectral measurements which indicate lower concentrations of H-α, N-I and O-I (Fig. 12c, vide infra).

With the focus above and at the graphite surface, time-resolved spectra indicate that the decay of air species and production of CN and N_2^+ are similar in time (Figs. 12a and 12b), with CN emission decaying less rapidly than H-α, N-I and O-I emission (plotted for "focus above" in Fig. 12d). With the laser focus moved to 2 mm below the graphite surface (Fig. 12c), less air is entrained in the plasma. H-α, N-I and O-I are not prominent in the spectra, and the shock wave is not axially elongated nor indicative of air- and substrate-borne shocks which fuse together. CN emission is also less persistent.

In Fig. 12e the intensity of CN (at 388 nm) vs. time with the focus above, at, and below the surface is compared. Differences are most pronounced with the laser focus below the surface. The faster decay of CN with focus below the surface may be due to decreased availability of reactive nitrogen (the ionization potential of N_2 is 15.581 eV and its production, by multiphoton ionization, will be very sensitive to laser intensity). There may also be more efficient scavenging of the CN radical at or near the surface. The decreased continuum emission contribution with focus below the surface (Fig. 12c vs. Figs. 12a and 12b) is consistent with the laser power density being lower in the observed region than when the focus is in the air or at the surface of the substrate. More C_2 is also observed with the focus below the surface. This may be due to there being fewer competing signatures, but is also consistent with lower power density. Sánchez-Aké et al.[50] observed more C_2 at lower flux and attributed it to the layer-by-layer ablation of graphite and production of C_n (n >2) carbon clusters, which dissociate to C_2 after collisions with energetic electrons. At higher fluences, the probability of direct C_n formation is decreased.

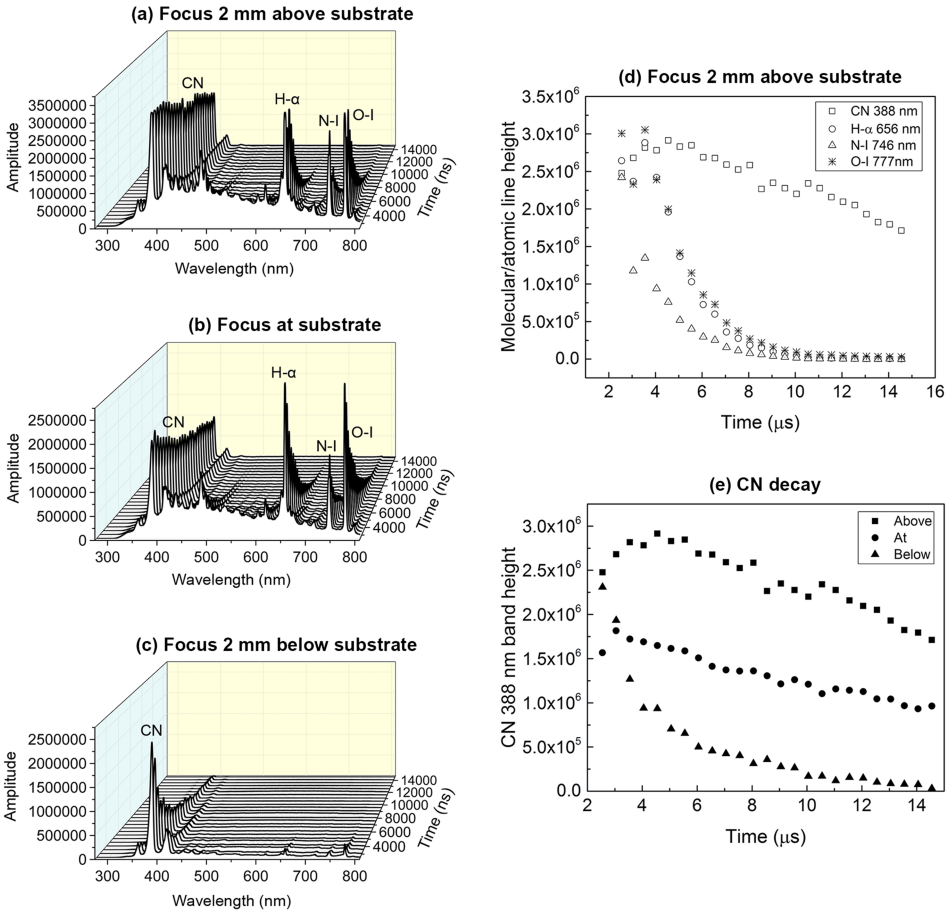

FIG. 12. Time-resolved spectra with the laser focus (a) 2 mm above the graphite substrate, (b) at the surface of the substrate, and (c) 2 mm below the substrate. The relative decays in molecular and atomic line heights with the focus 2 mm above the substrate are plotted in (d) and the decay of CN is compared with laser focus, above, at, and below the substrate surface in (e).

IV. CONCLUSIONS

Laser-induced breakdown spectroscopy is a powerful technique with readily variable parameters that can be used to simulate characteristics of detonations and high-temperature combustion. The temperatures and decay behavior of atomic aluminum and AlO emission resulting from laser ablation of an aluminum substrate are similar to those following detonation of a small quantity of aluminized explosive (20 g PBXN-113, work by Carney et al.[6]). For an Al-encased high explosive detonated in the field, the temperature at which AlO appears is similar, but the persistence of Al and AlO emission differs by two orders of magnitude. Simulations indicate that the temperature from AlO, 2 μs after laser ablation of Al in air, is ~4400 K ±100 K. This is in line with the temperature at which AlO formation is favored thermodynamically. In the field the apparent temperature of the spatially integrated AlO was roughly 3700 K between ~2 to ~4 ms following detonation. With respect to the impact of shocked air and the effect of combustion induced carbon, at 10 μs following laser-induced breakdown of air, in the 370 nm to 480 nm range, N_2^+ is the dominant molecular species (N_2^+:CN ~5:1), whereas with laser ablation of graphite in air CN is dominant (N_2^+:CN ~1:20). For sparked air a simulated plasma temperature of 7800 K provided the best fit of the experimental spectrum in the spectral range from 362 to 453 nm. With graphite present, the temperature appears to be lower, but not significantly so. For plasmas created by altering the ablating laser focus in relation to a graphite substrate in air, laser intensity appears to be a critical factor in CN production, and CN decay is more rapid with the focus below the surface of the sample.

Analogies with laser plasmas can help guide HE field measurements to spectral ranges, resolutions, and gate widths that have the greatest impact in terms of extracting relevant parameters from large-scale HE field test data. This work with Al, graphite and sparked air suggests parameters which could be derived from species observed at HE field tests in the UV, where blackbody and solar emissions are lower (particularly in the solar-blind region (230–290 nm)). For example, with sufficiently narrow gate widths and sufficiently high spectral resolution, it may be possible to derive: 1.) temperature from pairs of Al species (Al-I: $3s^2 3d\ ^2D \rightarrow 3s^2 3p\ ^2P^0$ transition at 308.2 and $3s^2 4s\ ^2S \rightarrow 3s^2 3p\ ^2P^0$ transition at 396.1 nm; and Al-II: $3s4f\ ^1F^0 \rightarrow 3p^2\ ^1D$ transitions at 263.15 nm and $3s4s\ ^1S \rightarrow 3s3p\ ^1P^0$ at 281.6 nm), 2.) temperature from molecular emissions (e.g., cyano-radical [CN violet system between $B^2\Sigma^+$ and $X^2\Sigma^+$ molecular states, ~340–425 nm]; and nitrogen monopositive ion N_2^+ [first negative system between $B^2\Sigma^+$ and $X^2\Sigma^+$ molecular states, ~340–480 nm]) and 3.) electron density via Stark broadening (e.g., Al-II $3s4s\ ^1S \rightarrow 3s3p\ ^1P^0$ transition at 281.6 nm). Species of interest to RF modelers seeking to identify sources of radiofrequency emissions may also be observed. As with the temperature derivations from the AlO emission at the HE field test, the effects of self-absorption must be considered, and when applicable, emissions from, and absorptions by other interfering species will need to be accounted for.

ACKNOWLEDGMENTS

We gratefully acknowledge Mary O'Neill for her contributions to obtaining a temperature fit for the field spectrum, and John Di Benedetto and Howard Bender for their insights and support. We also thank Daryl Dagel and Olga Blum Spahn for helpful discussions, as well as Ben Valencia, Rick Allison and Glen Anthony for assistance in the laser ablation chamber construction and sample preparation. This work was performed under the auspices of the U.S. Department of Energy, National Nuclear Security Administration by National Security Technologies, LLC, under Contract No. DE-AC52-06NA25946 (DOE/NV/25946–3186) and under Contract No. DE-AC02-05CH11231 at the Lawrence Berkeley National Laboratory. Financial support was provided by the Site Directed Research and Development Program (SDRD) of National Security Technologies, LLC, and by the U.S. DOE, Office of Defense Nuclear Nonproliferation Research and Development (NA-22).

necessarily represent the views of the U.S. Department of Energy or the United States Government. DOE/NV/25946–3303.

[1] K. C. Gross, J. Wayman, and G. P. Perram, "Phenomenological fireball model for remote identification of high-explosives," Proc. SPIE **6566**, 656613 (2007).
[2] J. E. Fine, "Estimates of the electromagnetic radiation from detonation of conventional explosives," Army Research Laboratory, Adelphi, MD, ARL-TR-2447 (2001).
[3] J. Harlin and R. Nemzek, "Physical properties of conventional explosives deduced from radio frequency emissions," Propellants Explos. Pyrotech. **34**, 544 (2009).
[4] L. S. Lebel, P. Brousseau, L. Erhardt, and W. S. Andrews, "Measurements of the temperature inside an explosive fireball," J. Appl. Mech. **80**, 031702 (2013).
[5] V. Bouyer, I. Darbord, P. Hervé, G. Baudin, C. Le Gallic, F. Clément, and G. Chavent, "Shock-to-detonation transition of nitromethane: Time-resolved emission spectroscopy measurements," Combustion and Flame **144**, 139 (2006).
[6] J. R. Carney, J. S. Miller, J. C. Gump, and G. I. Pangilinan, "Time-resolved optical measurements of the post-detonation combustion of aluminized explosives," Rev. Sci. Instrum. **77**, 063103-1–063103-6 (2006).
[7] J. R. Carney, J. M. Lightstone, T. P. McGrath II, and R. J. Lee, "Fuel-rich explosive energy release: Oxidizer concentration dependence," Propellants Explos. Pyrotech. **34**, 331 (2009).
[8] J. R. Carney and J. Wilkinson, "Atmospheric effects on time-resolved emission measurements of detonation of combustion products," 13th International Detonation Symposium, July 23–28, 2006, Norfolk VA, USA.
[9] J. M. Peuker, P. Lynch, H. Krier, and N. Glumac, "On AlO emission spectroscopy as a diagnostic in energetic materials testing," Propellants Explos. Pyrotech. **38**, 577 (2013).
[10] S. K. Monfared, D. M. Oro, M. Grover, J. E. Hammerberg, B. M. La Lone, C. L. Pack, M. M. Schauer, G. D. Stevens, J. B. Stone, W. D. Turley, and W. T. Buttler, "Experimental observations on the links between surface perturbation parameters and shock-induced mass ejection," J. Appl. Phys. **116**, 063504 (2014).
[11] J. J. Kay, R. R. Wixom, A. J. Brook, R. Knepper, A. S. Tappan, and D. L. Damm, "Spectroscopic analysis of time-resolved emission from detonating thin film explosive samples," Shock Compression of Condensed Matter - 2015, AIP Conf. Proc. **1793**, 030002-1 (2017).
[12] O. Ram and O. Sadot, "Implementation of the exploding wire technique to study blast-wave–structure interaction," Exp. Fluids **53**, 1335 (2012).
[13] M. N. Skaggs, M. J. Hargather, and M. A. Cooper, "Characterizing pyrotechnic igniter output with high-speed schlieren imaging," Shock Waves **27**, 15 (2017).
[14] C. Y. Liu, X. L. Mao, R. Greif, and R. E. Russo, "Time resolved shadowgraph images of silicon during laser ablation: Shockwaves and particle generation," J. Phys.: Conf. Ser. **59**, 338 (2007).
[15] J. L. Gottfried, "Laboratory-scale method for estimating explosive performance from laser-induced shock waves," Propellants Explos. Pyrotech. **40**, 674 (2015).
[16] S. S. Harilal, B. E. Brumfield, and M. C. Phillips, "Lifecycle of laser-produced air sparks," Phys. Plasmas **22**, 063301 (2015).
[17] S. S. Harilal, B. E. Brumfield, B. D. Cannon, and M. C. Phillips, "Shock wave mediated plume chemistry for molecular formation in laser ablation plasmas," Anal. Chem. **88**, 2296 (2016).
[18] A. Gupta, B. Braren, K. G. Casey, B. W. Hussey, and R. Kelly, "Direct imaging of the fragments produced during excimer laser ablation of $YBa_2Cu_3O_{7-\Delta}$," Appl. Phys. Lett. **59**, 1302 (1991).
[19] S. H. Jeong, R. Greif, and R. E. Russo, "Shock wave and material vapour plume propagation during excimer laser ablation of aluminum samples," J. Phys. D. Appl. Phys. **32**, 2578 (1999).
[20] X. Zeng, X. L. Mao, R. Greif, and R. E. Russo, "Experimental investigation of ablation efficiency and plasma expansion during femtosecond and nanosecond laser ablation of silicon," Appl. Phys. A **80**, 237 (2005).
[21] J. L. Gottfried, "Laser-induced plasma chemistry of the explosive RDX with various metal nanoparticles," Appl. Opt. **51**, B13 (2012).
[22] X. Mao, A. A. Bol'shakov, D. L. Perry, O. Sorkhabi, and R. E. Russo, "Laser ablation molecular isotopic spectrometry: Parameter influence on boron isotope measurements," Spectrochim. Acta B **66**, 604 (2011).
[23] P. Pořízka, B. Klessen, J. Kaiser, I. Gornushkin, U. Panne, and J. Riedel, "High repetition rate laser-induced breakdown spectroscopy using acousto-optically gated detection," Rev. Sci. Instrum. **85**, 073104 (2014).
[24] H. R. Griem, *Plasma Spectroscopy* (McGraw-Hill, New York, 1964).
[25] M. M. Litvak and D. Edwards, "7A8-Spectroscopic studies of laser-produced hydrogen plasma," IEEE J. Quantum Electronics **2**, 486 (1966).
[26] C. David, P. V. Avizonis, H. Weichel, C. Bruce, and K. D. Pyatt, "7A9-Density and temperature of a laser induced plasma," IEEE J. Quantum Electronics **2**, 493 (1966).
[27] B. C. Boland, F. E. Irons, and R. W. P. McWhirter, "A spectroscopic study of the plasma generated by the laser from polyethylene," J. Phys. B **2**, 1180 (1968).
[28] J. T. Knudtson, W. B. Green, and D. G. Sutton, "The UV-visible spectroscopy of laser-produced aluminum plasmas," J. Appl. Phys. **61**, 4771 (1988).
[29] A. L. Kuhl, "On the structure of self-similar detonation waves in TNT charges," Combust. Explos. Shock Waves **51**, 72 (2015).
[30] A. L. Kuhl, D. A. White, and B. A. Kirkendall, "Electromagnetic waves from TNT explosions," J. Electromagn. Anal. Appl. **6**, 280 (2014).
[31] R. J. Nordstrom, "Study of laser-induced plasma emission spectra of N_2, O_2, and ambient air in the region 350 nm to 950 nm," Appl. Spec. **49**, 1490 (1995).
[32] F. R. Gilmore, "Equilibrium composition and thermodynamic properties of air to 24 000 K," Rand Corp. Report RM-1543, (1955).

[33] C. O. Laux, T. G. Spence, C. H. Kruger, and R. N. Zare, "Optical diagnostics of atmospheric pressure air plasmas," Plasma Sources Sci. and Technol. **12**, 125 (2003).
[34] A. P. Boronin, V. N. Kapinos, S. A. Krenev, and V. N. Mineev, "Physical mechanism of electromagnetic field generation during the explosion of condensed explosive charges. Survey of literature," Combust. Explos. Shock Waves **26**, 597 (1990).
[35] J. E. Fine and S. J. Vinci, "Causes of electromagnetic radiation from detonation of conventional explosives: A literature survey," Army Research Laboratory, Adelphi, MD, ARL-TR-1690 (1998).
[36] P. W. J. M. Boumans, *Inductively Coupled Plasma Emission Spectroscopy, Part 2: Applications and Fundamentals* (Wiley, New York, 1987), 373.
[37] X. Bai, V. Motto-Ros, W. Lei, L. Zheng, and J. Yu, "Experimental determination of the temperature range of AlO molecular emission in laser-induced aluminum plasma in air," Spectrochim. Acta, B **99**, 193 (2014).
[38] A. T. Patrascu, S. N. Yurchenko, and J. Tennyson, "ExoMol molecular line lists: IX. The spectrum of AlO," Mon. Not. R. Astron. Soc. **449**, 3613 (2015).
[39] M. R. Dong, X. Mao, J. J. Gonzalez, J. D. Lu, and R. E. Russo, "Time-resolved LIBS of atomic and molecular carbon from coal in air, argon and helium," J. Anal. Atom. Spectrom. **27**, 2066 (2012).
[40] A. Anders, *A Formulary for Plasma Physics* (Akademie-Verlag, Berlin, 1990), 183.
[41] T. N. Piehler, F. C. DeLucia, Jr., C. A. Munson, B. E. Homan, A. W. Miziolek, and K. L. McNesby, "Temporal evolution of the laser-induced breakdown spectroscopy spectrum of aluminum metal in different bath gases," Appl. Opt. **44**, 3654 (2005).
[42] N. Konjević, A. Lesage, J. R. Fuhr, and W. L. Wiese, "Experimental stark widths and shifts for spectral lines of neutral and ionized atoms (A critical review of selected data for the period 1989 through 2000)," J. Phys. Chem. Ref. Data **31**, 819 (2002).
[43] S. A. S. Spectralfit, SPECAIR Version 3.0.2.0, http://SPECAIR-radiation.net/ (accessed August 2015).
[44] P. Boubert and P. Vervisch, "CN spectroscopy and physico-chemistry in the boundary layer of a C/SiC tile in a low pressure nitrogen/carbon dioxide plasma flow," J. Chem. Phys. **112**, 10482 (2000).
[45] A. Fernandez-Bravo, T. Delgado, P. Lucena, and J. J. Laserna, "Vibrational emission analysis of the CN molecules in laser-induced breakdown spectroscopy of organic compounds," Spectrochim. Acta, B **89**, 77 (2013).
[46] S. S. Harilal, A. Hassanein, and M. Polek, "Late-time particle emission from laser-produced graphite plasma," J. Appl. Phys. **110**, 053301-1 (2011).
[47] G. Dinescu, E. Aldea, M. L. De Giorgi, A. Luches, A. Perrone, and A. Zocco, "Optical emission spectroscopy of molecular species in plasma induced by laser ablation of carbon in nitrogen," Appl. Surface Science **127-129**, 697 (1998).
[48] M. Dong, J. Lu, S. Yao, Z. Zhong, J. Li, J. Li, and W. Lu, "Experimental study on the characteristics of molecular emission spectroscopy for the analysis of solid materials containing C and N," Optics Express **19**, 17021-1 (2011).
[49] M. Dong, G. C.-Y. Chan, X. Mao, J. J. Gonzalez, J. Lu, and R. E. Russo, "Elucidation of the C_2 and CN formation mechanisms in laser-induced plasmas through correlation analysis of carbon isotopic ratio," Spectrochim. Acta B **100**, 62 (2014).
[50] C. Sánchez-Aké, M. Bolaños, and C. Z. Ramirez, "Emission enhancement using two orthogonal targets in double pulse laser-induced breakdown spectroscopy," Spectrochim. Acta B **64**, 857 (2009).